Band Alignment and Photoresponse of LaFeO$_3$-Based Heterojunctions

Yunwei Sheng[�ID],[1] Mathieu Mirjolet[ID],[1] Mario Villa[ID],[1] Jaume Gàzquez[ID],[1] José Santiso[ID],[2]
Andreas Klein,[3] Jordi Fraxedas[ID],[2] and Josep Fontcuberta[ID][1,*]

[1]*Institut de Ciència de Materials de Barcelona (ICMAB-CSIC), Campus UAB, Bellaterra, Catalonia, 08193, Spain*
[2]*Institut Català de Nanociència i Nanotecnologia (ICN2 − CSIC & BIST) Campus UAB, Bellaterra 08193,
Catalonia, Spain*
[3]*Technische Universität Darmstadt, Institute of Materials Science, Otto-Berndt-Str. 3, 64287 Darmstadt, Germany*

Epitaxial LaFeO$_3$ (LFO)-based photocells, of different thicknesses (50–200 nm) have been grown on cubic LSAT (001) [(LaAlO$_3$)$_{0.3}$(Sr$_2$TaAlO$_6$)$_{0.7}$] single-crystal substrates, using a La$_{2/3}$Sr$_{1/3}$MnO$_3$ (LSMO) bottom electrode and different top electrodes [Pt, Ba$_{0.95}$La$_{0.05}$SnO$_3$ (BLSO)], to determine their photoresponse. The measured short-circuit photocurrent first increases with LFO thickness and then decreases, and it is larger or smaller, when Pt or BLSO electrodes are used, respectively. The corresponding open-circuit voltage displays the opposite trend, being smaller or larger for Pt and BLSO, respectively, which is in excellent agreement with the electronic band alignments determined by x-ray photoelectron spectroscopy and also consistent with the rectifying character of the dark current-voltage data. It turns out that the films display a complex microstructure containing different variants, strained and relaxed, of the orthorhombic LaFeO$_3$, that evolves with film thickness and entails the presence of strain gradients and, possibly, flexoelectric fields. We discuss these data and propose that the unavoidable grain boundaries between differently textured LaFeO$_3$ crystallites play a significant role on the observed responsivity (2.6×10^{-4} A W^{-1}), found to be larger than in related LFO-based structures.

I. INTRODUCTION

Narrow-band oxides are receiving tremendous attention in different areas of research and technology, which range from photoconversion and water splitting to spintronics [1]. To reach an efficient charge extraction, thin films of these oxides are usually grown between a bottom electrode or conducting substrate and a top metallic layer. The band alignment among the different layers is instrumental for device operation, as it determines the presence of valence-band and conduction-band offsets (VBO-CBO), implying the presence of built-in potentials across the structure. Selection of the electrodes is the simplest tool to adjust band alignments, via their work function. However, the interfaces between consecutive layers, metallic electrodes, and photoabsorbing layer, are not electronically rigid but are by themselves a device, where electronic reconstructions and interfacial dipoles may exist largely impacting the band alignment. For instance, focusing on narrow band-gap transition metal perovskites, such as LaFeO$_3$ (LFO), it was proposed that when LFO is grown on a large band-gap SrTiO$_3$ (STO) perovskite, a polar-nonpolar interface exists and thus charge discontinuity may arise at

the interface. Indeed, Nakamura *et al*. [2] and Nakamura *et al*. [3] observed that the photocurrent in LFO//STO heterostructures could be reversed by changing the atomic termination of the STO substrate and proposed the existence of an interface-induced polarization contributing to the photocurrent. Subsequent experiments did not allow evidence an atomic termination-dependent built-in dipole at the LFO//STO interface [4] but rather the presence of chemical instabilities at this interface, suggesting that details of the growth may be crucial [5].

In recent years, a different aspect of epitaxial heterostructure has emerged. Indeed, while the possible presence of strain gradients in thin films was well understood [6], the impact of the associated flexoelectric fields (E_f) on the photoresponse is now under scrutiny. The presence of strain gradients implies the presence of charge polarization in the dielectric layer and the associated flexoelectric field. In thin films, the contribution of E_f may be dramatic, as strain gradients can be exceedingly large (up to 10^7 m^{-1}), and could lead to voltages across the device comparable to built-in potentials and thus largely impacting band alignment. It follows that charge extraction could be governed by strain gradients. Illustrative examples include ferroelectric HoMnO$_3$ thin films, where strain gradient-related flexoelectric fields produce remarkable shifts of the ferroic

*fontcuberta@icmab.cat

loops [7] and, subsequently, modify the rectifying character of charge transport [8,9], or even the tunnel transport across dielectric barriers [10].

While $HoMnO_3$ in the above examples is ferroelectric, flexoelectricity is not restricted to polar materials but it should also exist in any centrosymmetric system under strain gradient, as nicely evidenced by the observation of the so-called flexophotovoltaic response in tip-deformed silicon [11]. The presence of the flexoelectric field has also been recently invoked to explain the relatively large photoresponse of ultrathin LFO films grown on substrates imposing a compressive strain ($LaAlO_3$, LAO) and attributed to a reduction of the height of the Schottky barrier at dielectric-metal interface, which favors charge extraction [12]. Interestingly, the benefiting effect of E_f is found to be maximal for ultrathin films (≤ 35 nm), where the largest short-circuit current density ($J_{SC} = 1.5$ mA cm^{-2}) is measured, but reducing at larger thicknesses, presumably due to a detrimental effect of dislocations and other plastic deformations resulting from strain relaxation which limit the photocarrier mean free path. By the same token, E_f is argued to be negligible in films grown on well-matched substrates (i.e., STO), where strain gradients should be minimal. In a further twist a photovoltaic-flexoelectric possible synergy, Jiang *et al.* reported on tunable photoresponse of LFO films grown on flexible substrates (mica), proposing that the effect is due to strain gradient-controlled bending of the films [13]. While at first sight the possible effect of strain gradients on the modulation of interfacial Schottky barriers seems well supported by the observed changes of J_{SC}, still questions arise regarding the open-circuit voltage (V_{OC}) values in strain-graded samples. The flexoelectric field E_f along a given direction (e.g., z) is roughly expressed by

$$E_f \approx N \frac{q}{a} \frac{1}{\varepsilon_0} \frac{\partial \epsilon}{\partial z},$$

where N is a scaling factor depending on the material (approximately equal to 1 in perovskite oxides) [14], q is the elementary charge, a is the cell parameter, ε_0 is the vacuum permittivity, and the derivative term is the gradient of strain (ε) along the z axis. Using $N = 1$, and the reported strain gradient ($\partial \varepsilon / \partial z$) $\approx 10^6$ for a 35-nm LFO film on LAO [12], it turns out that $E_f \approx 4.5 \times 10^7$ V/m, corresponding to a contribution to the built-in potential (V_{BI}) of about V_f (flexoelectric potential) ≈ 1.6 eV. In these structures, V_{OC} is primarily bounded by the built-in potential and consequently depends on the metal electrodes and typically is much smaller ($V_{BI} \approx 0.2$–0.8 eV) [12] than V_f. As V_f is predicted to be larger than V_{BI}, it follows that V_{OC} should be dramatically modified by E_f and even the sign could be reversed depending on strain gradient. However, reported data on strain-graded structures evidence minor variations of V_{OC} with strain gradient [12,13], suggesting that the scenario is more intricate.

Here, aiming at getting a deeper understanding of the complex interplay of different effects contributing to band alignment and photoresponse in narrow-band oxides, we report on the conductivity, band alignment, and photoresponse of LSMO/LFO/M heterostructures where the LFO layer is 50–200 nm thick, and M are different top metallic layers (Pt and BLSO), and $La_{2/3}Sr_{1/3}MnO_3$ (LSMO) is a common bottom electrode in the structure. As a substrate, we select LSAT [$(LaAlO_3)_{0.3}(Sr_2TaAlO_6)_{0.7}$], which is cubic and has a cell parameter intermediate to those of the above-mentioned STO and LAO and that should give rise to a different strain-gradient pattern in LFO films. As the bulk LFO cell is orthorhombic in nature, the growth of LFO on relatively well-matched cubic substrates is expected to lead to crystallites with different orientations of the longest orthorhombic axis with respect to the substrate and, concomitantly, the film microstructure should be relatively complex, as we report. It is found that the charge transport across the heterostructure and the photoresponse are mainly controlled by the band alignments, that set both the interfacial built-in potential V_{BI} across the various interfaces and the observed open-circuit voltage V_{OC}, with obvious differences depending on the work function of the top metallic electrodes, without a governing role of flexoelectric fields. Remarkably, it is found that the J_{SC} of these structures can be larger than in ultrathin LFO films where flexoelectric contribution was invoked [12]. We suggest a different scenario in which grain boundaries, as seen in $BiFeO_3$ [9], largely contribute to the observed enhanced photoresponse.

II. METHODS

A. Sample preparation

Single layers of $LaFeO_3$ (LFO) are first deposited by pulsed laser deposition (PLD) on $Nb:SrTiO_3(001)$ substrates to determine the optimal growth conditions. Next, metal-insulator-metal heterostructures are grown on LSAT (001), where the photoabsorbing LFO (insulator) is sandwiched between the bottom electrode (BE): $La_{2/3}Sr_{1/3}MnO_3$ (LSMO), and a top metallic electrode (TE). Two different materials are investigated as TE: semi-transparent Pt and transparent $Ba_{0.95}La_{0.05}SnO_3$ (BLSO). Dedicated ultrathin, up to few nanometers thick, LFO, Pt, and BLSO films are grown for band-alignment measurements (see below).

B. Structural characterization

Phase purity and cell parameters (out-of-plane and in-plane) are measured by x-ray diffraction using a X'Pert Pro MRD diffractometer, Malvern-Panalytical [θ–2θ scans, reciprocal space maps (RSMs)]. Cross-section scanning

transmission electron microscopy (STEM) analysis of LSAT//LSMO/LFO heterostructures is performed using a probe aberration corrected Jeol ARM 200cF STEM with a cold field emission source operated at 200 kV.

C. Band-alignment determination

The band alignment at the metal-insulator (or insulator-metal) interfaces are determined by x-ray photoelectron spectroscopy (XPS) combined with ellipsometry measurements for band-gap evaluation. The valence-band offset (VBO) is determined by measuring energy differences associated to two different core levels characteristic of each material and their relative position to the corresponding valence-band maximum (VBM) [15,16].

D. Electrical measurements and photoresponse

Two-point-probes current-voltage (I-V) characteristics are recorded in top-bottom configuration (the LSMO bottom electrode is connected to the ground), where positive current corresponds to positive charges flowing from TE towards the BE. I-V characteristics under illumination are collected mainly using a monochromatic blue laser ($\lambda = 405$ nm, $h\upsilon = 3.06$ eV) with power density $I_0 \approx 54$ W cm^{-2} (beam diameter $S_d \approx 280$ μm). The photoresponse dependence on wavelength (λ) is recorded by using a STEC multiwavelength system (Blue Sky Research), with a parallel laser beam of $\lambda = 405$, 450, 520, and 638 nm ($S_d \approx 1.7$ mm, $I_0 \approx 0.55$ W cm^{-2}). The incidence angle is fixed at 45°.

For details of methods see section S1 within the Supplemental Material [17].

III. RESULTS

A. Structural data

X-ray diffraction θ–2θ scans and reciprocal space maps (RSM) are collected on LSMO/LFO/Pt and LSMO/LFO/BLSO heterostructures, having different thicknesses of the LFO (t_{LFO}) photoabsorbing layer. The RSM (Fig. 1) clearly show that LSMO is fully epitaxial and coherently grown on LSAT(001). In contrast, LFO displays more complex diffraction patterns that arise from the coexistence of fully strained and gradually relaxing crystallites of LFO differently textured on LSAT//LSMO. Bulk LFO has an orthorhombic structure *Pbnm* (62) with room-temperature cell parameters $a = 5.5544$ Å, $b = 5.5659$ Å, and $c = 7.8534$ Å [18], that correspond to pseudotetragonal c(LFO) = 3.9267 Å and a(LFO) = 3.9316 Å interplanar distances. The cell parameter of LSAT is 3.868 Å, and accordingly the mismatch is only marginally smaller (-1.5%) when c(LSAT)//c(LFO) than when c(LSAT)//a(LFO) (-1.6%). Therefore, it can be expected that LFO film grows with crystallites having their c axis in the (001) plane of LSAT//LSMO (denoted
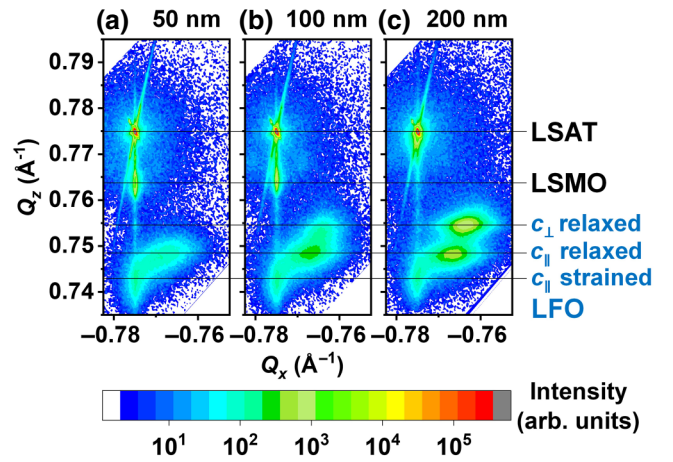

FIG. 1. (a)–(c) Reciprocal space maps around the (−303) reflection of LSAT of LSMO/LFO/Pt heterostructures having $t_{LFO} = 50$, 100, and 200 nm, respectively. Horizontal lines indicate out-of-plane position of the diffracting planes of LSAT, LSMO, and the position of the observed fully strained and relaxed $c_{\parallel}$ crystallites, and relaxed $c_{\parallel}$ ones, of LFO.

as $c_{\parallel}$), either clamped to the substrate or gradually relaxing when increasing thickness, somehow mixed with LFO crystallites with c(LSAT)//a(LFO) (denoted as $c_{\perp}$). The RSM of the $t_{LFO} \approx 50$ nm film, displays a fraction of coherently grown LFO crystallites (horizontal line in Fig. 1), as mentioned most likely with their c axis in plane ($c_{\parallel}$), and a fraction of relaxed phase (horizontal line in Fig. 1). The relative fraction of the relaxed phase increases when the film thickness increases, as appreciated in $t_{LFO} \approx 100$ nm. For the thickest films ($t_{LFO} \approx 200$ nm) an additional diffraction spot appears in the RSM that fits well with the expected position of d (002) indicating a $c_{\perp}$-textured crystallite (Fig. S2.1 within the Supplemental Material [17]).

Therefore, the growth of relatively thick (50–200 nm) films of LFO on LSAT leads to a subtle coexistence of epitaxial crystallites of different texture, either coherently grown or relaxed as observed in Figs. 1(a)–1(c). The LFO microstructure observed in LSAT//LSMO/LFO structures having Pt and BLSO electrodes are found to be virtually identical (Fig. S2.2 within the Supplemental Material [17]).

The microstructure of LSMO(27 nm)/LFO(100 nm) heterostructure grown on LSAT is studied by means of STEM. LFO films present a columnar morphology, where continuous lines of low-angle grain boundaries propagate across the LFO layer, see Figs. 2 and S3.1 of the Supplemental Material S3 [17]. In addition, the LFO film shows misfit dislocations (see Fig. 2), suggesting these relatively thick films are relaxed. These results are in agreement with both x-ray measurements (Fig. 1) and electron diffraction patterns (Figs. S3.2 and S3.3 within the Supplemental Material [17]), which anticipate a rather

complex microstructure of the LFO films grown on LSAT. Figure 2(a) shows a high-resolution high-angle annular dark-field image (HAADF-STEM) image where different crystallographic domains propagate along the LFO layer. The domains can be distinguished using a local fast Fourier transform (FFT) as well. The red and green squares mark the areas from which FFTs have been obtained, and they correspond to domains with *c* perpendicular [Fig. 2(f)] and *c* parallel [Fig. 2(g)], to the interface, respectively. The orange circles of Fig. 2(g) mark the reflections that appear when the *c* axis lays in plane and allow for distinguishing different crystallographic domains (see also section S3 within the Supplemental Material [17]). One would expect that the high number of domain boundaries would generate local strain and defects throughout the LFO film. To get a new insight that low-angle annular dark field (LAADF) images are acquired, see Fig. 2(b). Notice that the LAADF-STEM image shows a bright contrast that progressively fades away near the surface of the film. Since the LAADF

contrast contains information of the strain [19,20], the images suggest that the lattice of the LFO film grown on LSAT present depth-wise deformations, or in other words, the lattice is much more relaxed away from the interface. Interestingly, the LAADF-STEM image also shows a homogeneous contrast at the bottom of the LFO film, which suggests a fully strained 8–9-nm-thick LFO layer that grows coherently with the LSMO buffer layer. Indeed, higher magnification HAADF and LAADF-STEM images [Figs. 2(c) and 2(d)] show that the brighter contrast at the base of the LFO columns appear just above this fine and strained LFO layer, and also that there are misfit dislocations atop this region. These results rule out the possibility that the observed difference in contrast is induced by a change in the thickness of the STEM specimen. Wrapping up, STEM results are in good agreement with the x-ray analysis of the strain of the films on LSAT, which unveiled not only a domain structure but also strained and relaxed regions within the LFO layer.
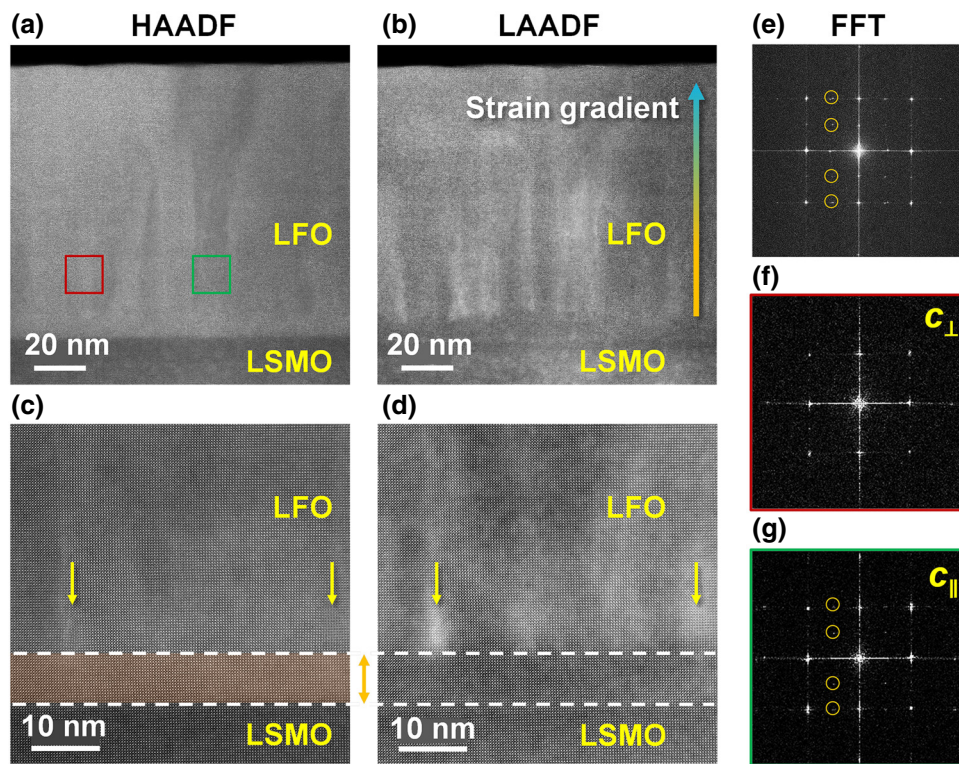

FIG. 2.   (a) HAADF-STEM and (b) LAADF-STEM images of a LSAT//LSMO(27 nm)/LFO(100 nm) heterostructure, respectively. As the contrast in a LAADF-STEM image contains information of strain, the image shows that near the LSMO/LFO interface the LFO is more distorted and that this distortion diminishes near the top surface. Notice that the contrast in the HAADF-STEM image is constant throughout the LFO film, and the minor variations in contrast are due to the existence of different crystallographic domains. Higher magnification (c) HAADF-STEM and (d) LAADF-STEM images, respectively. LAADF-STEM image shows a brighter contrast at the base of the LFO columns just above a thin and strained LFO layer, delimited with dashed white lines and an orange shadow in (c). The yellow arrows point at misfit dislocations located atop the strained LFO layer. FFTs belong to the (e) whole LFO film and to the (f) red and (g) green squares shown in (a), respectively. The orange circles in (e),(g) mark the reflections that appear when the *c* axis lays in plane.

B. *J-V* characteristics and LFO thickness dependence

In Figs. 3(a) and 3(c), we show the current density-voltage (*J-V*) curves of the LSMO/LFO/Pt and LSMO/LFO/BLSO heterostructures, respectively. These *J-V* curves are clearly not Ohmic. They display an asymmetric conductivity between negative and positive bias voltage, indicating a rectifying behavior that becomes more perceptible when increasing LFO thickness and more pronounced in LSMO/LFO/BLSO than in LSMO/LFO/Pt. Moreover, it can be appreciated that the conductivity decreases when the thickness of LFO increases, indicating that above some threshold voltage the conductivity is bulk-limited. Interface limited conductivity, as dictated by interfacial Schottky barriers at LSMO/LFO and LFO/(Pt, BLSO) interfaces, of height Φ_2 and Φ_1, would be prevalent at low voltages. In the interface-dominated regime, the LSMO/LFO/(Pt, BLSO) devices can be viewed as a back-to-back association of Schottky diodes [21] with a p-type (LFO) semiconductor, with an internal resistance (R_i) representing the carrier transport across the semiconducting LFO [22]. Inclusion of the R_i term is dictated by the observation that at relatively large voltages, the conductivity of the capacitors is clearly dependent on the thickness of the LFO layer. This model allows replication of [Figs. 3(b) and 3(d)] the experimental data for the thinnest LFO layer, to deduce the $\Phi_{1,2}$ energy barriers and, under the assumption that $\Phi_{1,2}$ are independent of the LFO thickness, to estimate the contribution of R_i. It turns out that Φ_1(LFO/Pt) ≈ 0.63 eV, Φ_1(LFO/BLSO) ≈ 1.1 eV and Φ_2(LSMO/LFO) ≈ 0.83 eV (section S4.1 within the Supplemental Material [17]). These results clearly confirm the presence of a larger and dissimilar Schottky barrier in LSMO/LFO/BLSO than in LMO/LFO/Pt, and account for the larger rectifying character of the former.

At high voltage, the space-charge-limited conduction (SCLC) mechanism predicts that $J \approx V^2$ and a power dependence on the LFO thickness, which is consistent with the observed variation with t_{LFO} of the extracted R_i values (section S4.2 within the Supplemental Material [17]).

The observed asymmetric *J-V* curves reflect the presence of a nonzero built-in potential V_{BI} through the LSMO/LFO/Pt and LSMO/LFO/BLSO structures. According to data in Figs. 3(a) and 3(c), and as deduced from the numerical analysis of the *J-V* curves, presumably V_{BI}(LSMO/LFO/BLSO) > V_{BI}(LSMO/LFO/Pt). When an insulating (or semiconducting) material is sandwiched between two metallic electrodes having work functions
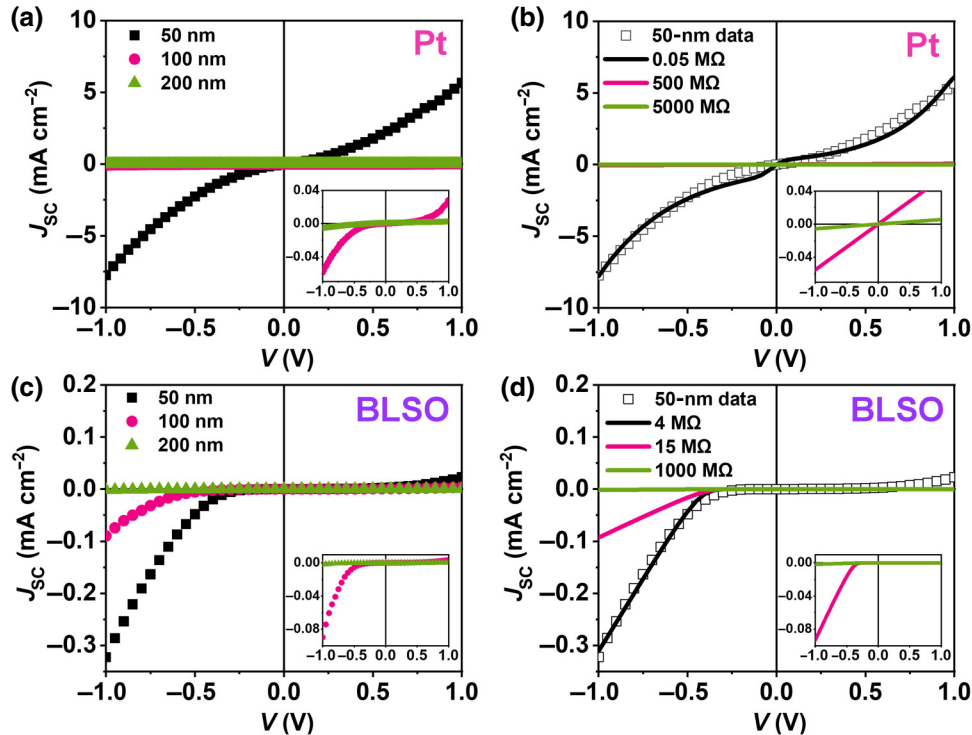

FIG. 3. *J-V* characteristics measured in dark of (a) LSMO/LFO/Pt and (c) LSMO/LFO/BLSO heterostructures, with varying LFO thickness of 50, 100, and 200 nm. Simulations of *J-V* curves in (a),(c) using the back-to-back diode model with an internal resistance (R_i) with varying LFO thickness are shown in (b) LSMO/LFO/Pt and (d) LSMO/LFO/BLSO. Black lines are the simulations of the experimental data (empty symbols) of the thinnest device ($t_{LFO} = 50$ nm), red and green lines are obtained with the same Schottky barrier parameters but increasing R_i.
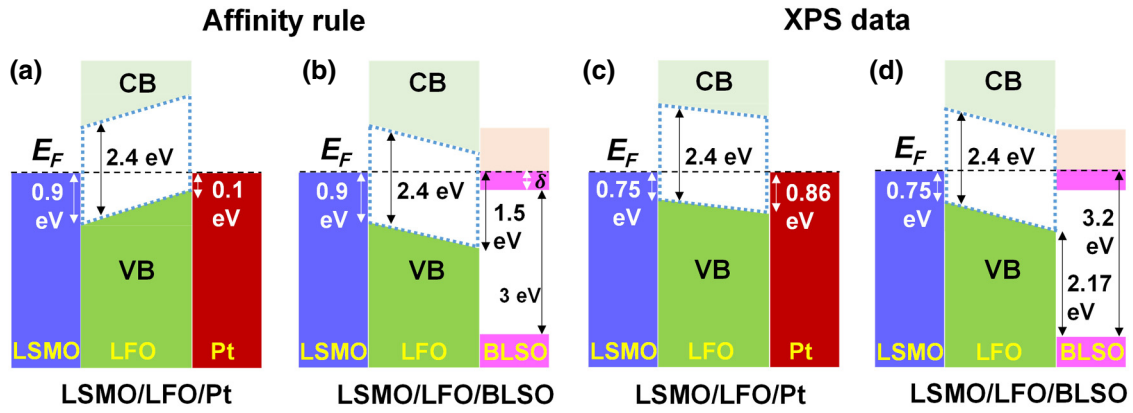
FIG. 4. Schematic energy band diagrams based of (a),(c) LSMO/LFO/Pt and (b),(d) LSMO/LFO/BLSO heterostructures, as inferred from the electron affinity rule (a),(b) and as deduced from XPS data (c),(d). The LFO layer is assumed to be fully depleted (flat bands) for sake of clarity. The band gaps of LFO and BLSO are indicated. The position of the Fermi level in BLSO, which is depending on the doping level (La^{3+}), is indicated in (b) by δ.

φ_1 and φ_2, a built-in potential V_{BI} emerges. The microscopic mechanism can be various as discussed in detail by Zhong and Hansmann [23]. In the simple electron *affinity-rule* (EAR, Anderson-Mott) approach [24], is given by $V_{BI} = (\varphi_1 - \varphi_2)/q$ [25], with q the positive elementary charge. Using the reported work function of LSMO ($\varphi_{LSMO} = 4.8$ eV) [26–28] and Pt ($\varphi_{Pt} = 5.6$ eV) [29–34], EAR predicts a built-in potential $V_{BI,th} = -0.8$ eV for LSMO/LFO/Pt. Using the reported electronic affinity of LFO ($\chi_{LFO} = 3.3$ eV [35]) and measured indirect band gap of our LFO films [E_g(indirect) ≈ 2.4 eV] (section S5 within the Supplemental Material [17]). The band alignment for LSMO/LFO/Pt derived within the electron affinity rule model is depicted in Fig. 4(a), where a rigid fully depleted flat band model is assumed. Similarly, using the $\varphi_{BLSO} = 4.2$ eV [36,37], EAR predicts $V_{BI,th} = +0.6$ eV and using the optically determined indirect band gap of BaSnO$_3$ (approximately equal to 3 eV [38,39]), the band alignment predicted within AER in LSMO/LFO/BLSO is shown in Fig. 4(b), where the Fermi level in BaSnO$_3$ has been shifted up above the conduction-band minimum by δ to illustrate the *n* doping of in BLSO.

It follows that the band alignment derived from AER display an opposite slope for LSMO/LFO/Pt and LSMO/LFO/BLSO capacitors that would imply a rectifying character of opposite sign, which is not observed. However, the AER model does not include electronic reconstructions arising from chemical bonding across the interfaces nor the presence of interfacial dipoles of Fermi-level pinning, it assumes sharp interfaces and no chemical interdiffusion, etc., has been largely criticized [23,24,32]. Similarly, the back-to-back diode model and the inclusion of the internal series resistance is far from unambiguous and energy barriers extracted from transport measurements may not be accurate enough [40]. Therefore, the valence-band offsets (VBOs) at the

interfaces between the different consecutive bilayers, namely LSMO/LFO, LFO/Pt, and LFO/BLSO interfaces, need to be directly measured to account for the *I-V* curves recorded in dark and for the photoresponse to be described latter. We use XPS and follow the methodology introduced by Kraut *et al.* [15,41] widely used to determine the VBO at oxide/oxide interfaces [4,38,42–46], or the Schottky barrier height at oxide/metal interfaces [40,47,48].

C. Band alignments

1. LSMO/LFO/Pt

To determine the VBOs at LSMO/LFO and LFO/Pt interfaces, we measure the valence-band maxima (E_{VBM}) of the different layers (LSMO, LFO, and Pt), first when separated and then when in intimate contact, using as reference the core levels (CLs) of various elements of the layers, to evaluate $\Delta E_{VBM}^{LSMO/LFO} = E_{VBM}^{LFO} - E_{VBM}^{LSMO}$ and $\Delta E_{VBM}^{LFO/Pt} = E_{VBM}^{Pt} - E_{VBM}^{LFO}$, respectively. By knowing the band gap of the materials, the relative position of their conduction-band minima (E_{CBM}) can also be deduced.

The LSMO/LFO interface is first investigated. To this aim, the position of various CLs relative to the corresponding valence-band maxima, in LSMO and LFO thick films (27 and 35 nm, respectively) grown on STO and Nb : STO substrates, respectively, are determined. Subsequently, the spectra of ultrathin LFO films (1, 3, 5 nm) on LSMO are collected and the energy position of CLs of the capping layer (LFO) and the bottom one (LSMO) are compared. Examples for Fe3*p* lines and Sr3*d* lines of LSMO/LFO(3 nm) are shown in Fig. 5(a). Next, XPS data of ultrathin Pt films (1, 3, 5 nm) grown on LFO are similarly measured and the positions of the corresponding core level (CL) are compared. Figures 5(b) and 5(c) show, as illustrative data, the Pt4*f* and La4*d* lines collected on
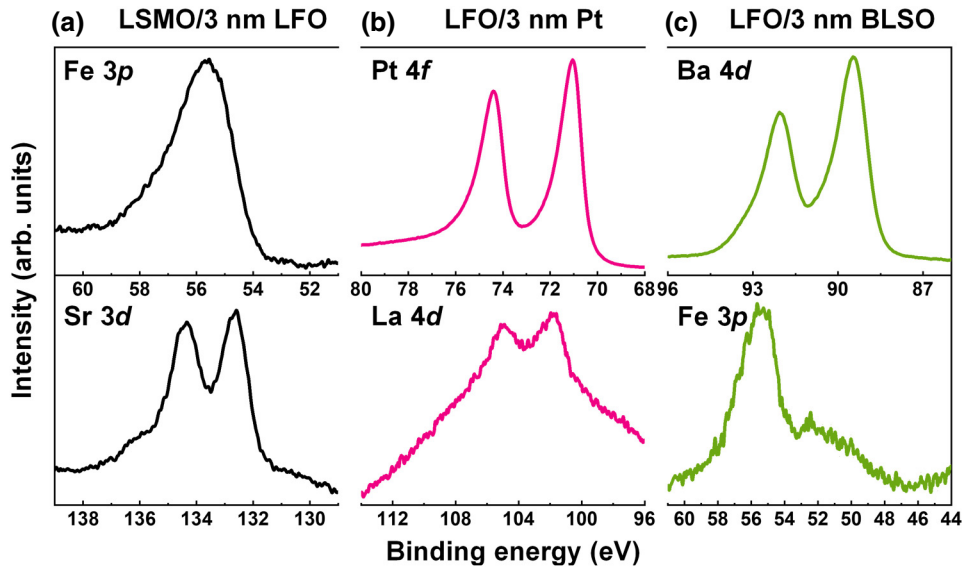
FIG. 5.   High-resolution XPS spectra of the selected pairs of core level lines for the determination of the corresponding band offsets for 3-nm-thick films of (a) LSMO (Sr3d)/LFO (Fe3p) (left), (b) LFO (La4d)/Pt (Pt4f) (middle) and (c) LFO (Fe3p)/BLSO (Ba4d) (right). The energies are referred to as the Fermi level of the analyzer.

LFO/Pt(3 nm) and the Ba4d and Fe3p lines collected on LFO/BLSO(3 nm), respectively. Data for other CLs and film thicknesses are provided in Fig. S6.3 within the Supplemental Material [17]. By collecting the values for two CLs of LFO (Fe2p and Fe3p) and two CLs of LSMO (Mn2p, Sr3d), up to four different VBO values can be extracted, by using Eq. (1).

$$\Delta E_{\text{VBM}} = (E_{\text{LFO-CL}} - E_{\text{VBM}})^{\text{thick-LFO}}$$
$$- (E_{\text{LSMO-CL}} - E_{\text{VBM}})^{\text{thick-LSMO}}$$
$$- (E_{\text{LFO-CL}} - E_{\text{LSMO-CL}})^{\text{interface}}. \quad (1)$$

Table I gathers the VBO (ΔE_{VBM}) values obtained using Eq. (1), for LSMO/LFO(3 nm), LFO/Pt(3 nm), and LFO/BLSO(3 nm). It is remarkable that the distribution of ΔE_{VBM} values around the mean value is notably narrow for LSMO/LFO and LFO/Pt.

The negative sign of ΔE_{VBM} ($\Delta E_{\text{VBM}} < 0$) for the bottom interface (LSMO/LFO) indicates that the $(E_{\text{VBM}})_{\text{LFO}}$

is below $(E_{\text{VBM}})_{\text{LSMO}}$. This result is in agreement with predictions made above on the basis of the electron affinity rule [24] applied to the band alignment at the LSMO/LFO interface [Fig. 4(a)]. It is also in qualitative agreement with the results of Smolin [49] *et al.* in related LaMnO$_3$/LFO interfaces, although fine details naturally differ as the electronic properties of the LaMnO$_3$ (semiconductor) and LSMO (metallic) layers are intrinsically dissimilar. ΔE_{VBM} data collected for other LFO thicknesses (Fig. S6.3 and Table S6 within the Supplemental Material [17]) consistently display this trend with minor variations on thickness.

Next, we analyze the top interface (LFO/Pt) using the same methodology. The PLD-deposited LFO (50 nm) film is transferred under UHV to the sputtering chamber for Pt deposition to avoid surface contamination. Different LFO/Pt (1 nm, 2 nm, 3 nm) heterostructures are deposited, and XPS is used to determine the position of several CL energies: Pt4f, La3d, Fe2p, and La4d. Use of Eq. (2) allows extraction of up to three VBO values for each sample

TABLE I.   Summary of VBOs measured at the LSMO/LFO(3 nm), LFO/Pt(3 nm) and LFO/BLSO(3 nm) interfaces as a function of LFO, Pt, and BLSO coverages. The VBOs are extracted from each pair of CLs, indicated by the corresponding column headings. Bold data correspond to spectra shown in Fig. 5. The last column gives the average values and data in brackets indicate the standard deviation of the average value. The "X" symbol indicates that a CL line is not perceptible in the XPS spectrum, and "XX" indicates that averaging is not appropriate due to differential charging effects.

LSMO/LFO	ΔE_{VBM} (eV)	Fe2p-Mn2p	Fe2p-Sr3d	Fe3p-Mn2p	**Fe3p-Sr3d**	Average
		−0.70	−0.72	−0.77	**−0.79**	−0.75 (0.04)
LFO/Pt	ΔE_{VBM} (eV)	Pt4f-La3d		Pt4f-Fe2p	**Pt4f-La4d**	Average
		0.89		X	**0.82**	0.86 (0.05)
LFO/BLSO	ΔE_{VBM} (eV)	Fe3p-Ba3d		Fe3p-Sn3d	**Fe3p-Ba4d**	Average
		−2.50		−2.45	**−2.17**	XX

(Table I).

$$\Delta E_{\text{VBM}} = (E_{\text{Pt-CL}} - E_{\text{VBM}})^{\text{thick-Pt}}$$
$$- (E_{\text{LFO-CL}} - E_{\text{VBM}})^{\text{thick-LFO}}$$
$$- (E_{\text{Pt-CL}} - E_{\text{LFO-CL}})^{\text{interface}}. \quad (2)$$

For LFO/Pt(3 nm), the Fe3p CL is found to be imperceptible in the XPS spectrum because the inelastic mean free path of electrons originating from this CL is shorter than the Pt thickness, thus precluding its use to determine ΔE_{VBM} (indicated by the "X" symbol in Table I). It can be appreciated in Table I that all data indicate a systematical shift between Pt and LFO CLs, with $\Delta E_{\text{VBM}} \approx 0.86$ (0.05) eV. The positive sign of ΔE_{VBM} ($\Delta E_{\text{VBM}} > 0$) indicates that the Fermi energy of Pt is above the VBM of LFO. ΔE_{VBM} data collected for other Pt thicknesses (Fig. S6.4 and Table S6 within the Supplemental Material [17]) consistently display this trend.

Using the VBO of LSMO/LFO and LFO/Pt (Table I), the band alignment of the LSMO/LFO/Pt structure is sketched in Fig. 4(c). Notice that according to the XPS data, there is a small build-in potential ($V_{\text{BI,XPS}}$) across the LSMO/LFO/Pt heterostructure with a value of $V_{\text{BI,XPS}} \approx (0.86 \text{ eV} - 0.75 \text{ eV}) \approx +0.11$ eV. Notice the XPS determined $V_{\text{BI,XPS}}$ (approximately equal to +0.11 eV) radically differs in sign from that obtained from the electron-affinity rule ($V_{\text{BI,th}} \approx -0.8$ eV) [Fig. 4(a)]. Such a discrepancy of band-alignment estimates using the electron-affinity rule and the experimental determinations is commonly observed when using Pt (or other metals) as the top electrode onto some oxide layers [40,47,48]. Of greatest interest here is that the band alignment measured in LSMO/LFO/Pt [Fig. 4(c)], indicating a small built-in potential is in agreement with the shape of J-V curves [Fig. 3(a)], which displays a rather symmetric behavior with minor rectification at $V < 0$.

2. LSMO/LFO/BLSO

A similar protocol is used to determine the band alignment in LSMO/LFO/BLSO. As the LSMO/LFO interface is identical to that explored in LSMO/LFO/Pt heterostructures described above, only additional measurements are done to deduce VBOs at the LFO/BLSO interface. With this aim, a thick BLSO (40 nm) film and ultrathin LFO/BLSO(2, 3 and 5 nm) films are measured. Several CLs are measured in BLSO (Ba3d, Sn3d, and Ba4d) and LFO (Fe2p and Fe3p). Illustrative CLs for LFO/BLSO(3 nm) are shown in Fig. 5(c). Data for other BLSO thicknesses are in Fig. S6.5, Table S6 within the Supplemental Material [17]. The VBOs are calculated

using Eq. (3) and are included in Table I.

$$\Delta E_{\text{VBM}} = (E_{\text{BLSO-CL}} - E_{\text{VBM}})^{\text{thick-BLSO}}$$
$$- (E_{\text{LFO-CL}} - E_{\text{VBM}})^{\text{thick-LFO}}$$
$$- (E_{\text{BLSO-CL}} - E_{\text{LFO-CL}})^{\text{interface}}. \quad (3)$$

The fact that the energy shift for all CL lines is not constant illustrates residual charging effects in the BLSO (3 nm) film grown on insulating LFO, which is negligible when evaluating the conducting LSMO/LFO/Pt interfaces. Indeed, charging effects are expected to be more evident when comparing CLs with a large difference in energies (for instance Fe3p-Ba3d) than for more reduced differences (Fe3p-Ba4d). Consequently, ΔE_{VBM} values in LFO/BLSO data in Table I are not averaged and ΔE_{VBM} (Fe3p-Ba4d) ≈ -2.17 eV is used for subsequent discussion. Charging is exacerbated in the thinnest BLSO film (2 nm, not shown) and reduced in the 5-nm film (Fig. S6.5 within the Supplemental Material [17]). The negative sign of $\Delta E_{\text{VBM}} \approx -2.17$ eV indicates that $(E_{\text{VBM}})_{\text{BLSO}}$ is below $(E_{\text{VBM}})_{\text{LFO}}$, as already anticipated from the affinity rule $[V_{\text{bi,th}}(\text{LFO/BLSO}) \approx -(1.5 + \delta)$ eV, Fig. 4(b)]. On the other hand, the position of the VBM in BSLO with respect to the Fermi level is found $E_{\text{VBM}} \approx -3.2$ eV (Fig. S6.5 within the Supplemental Material [17]), which is a good agreement with earlier reports [50,51] and the indirect gap determined from optical measurements [38,39]. Using these values, the experimentally determined band alignment is shown in Fig. 4(d), indicates $V_{\text{BI,XPS}} \approx +0.28$ eV for LSMO/LFO/BLSO. These results confirm the presence of a built-in potential in the LSMO/LFO/BLSO, of the same sign, slightly larger than in LSMO/LFO/Pt, which would induce a stronger rectification and higher conductance at $V < 0$ as observed in Fig. 3(c).

D. Photoresponse

1. Wavelength dependence of the photocurrent

The J-V characteristics in dark and under illumination of LSMO/LFO (100 nm)/Pt heterostructures recorded using different wavelengths are shown in Fig. 6(a). One can observe the emergence of a short-circuit current and the presence of an open-circuit voltage even with the red laser, which are fingerprints of photovoltaic effect in the visible range. As observed, J_{SC} largely increases when increasing the photon energy [left axis in Fig. 6(b)]. The abrupt increase of J_{sc} around 2.4–2.8 eV indicates that the band gap of LFO is within this range, which is in excellent agreement with energy-dependent absorption coefficient [yellow line, right axis in Fig. 6(b)] as derived from optical transmission experiments (section S5 within the Supplemental Material [17]) and literature data.
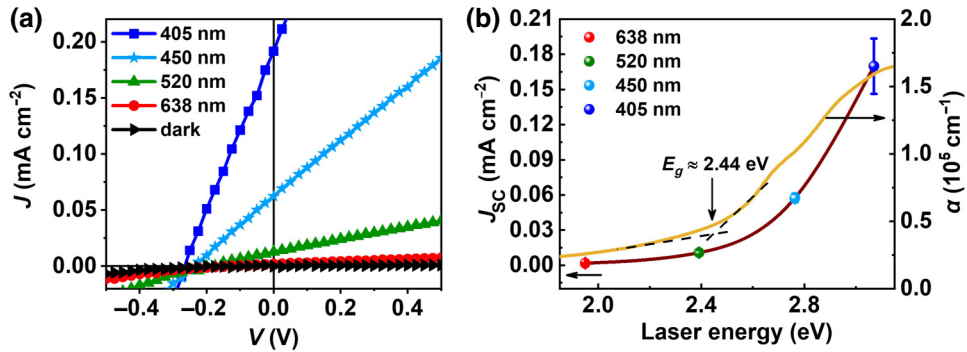
FIG. 6. (a) Photocurrent of LSMO/LFO(100 nm)/Pt measured in dark and using 0.55 W cm^{-2} lasers of different wavelength as indicated. (b) Dependence of the short-circuit photocurrent (left) and absorption coefficient α (right) on photon energy. Error bar indicates the spread of values recorded in various electrodes (up to 6) of the same diameter.

2. Photoresponse of LSMO/LFO/Pt and LSMO/LFO/BLSO

The photoresponse recorded using $\lambda = 405$ nm photons, of LSMO/LFO/Pt and LSMO/LFO/BLSO heterostructures of different thickness of the LFO photoabsorber (50, 100, and 200 nm) are shown in Figs. 7(a)–7(f), respectively. The thickness dependence of V_{OC} and J_{SC} are summarized in Figs. 8(a) and 8(b), respectively. We first notice in Figs. 7(a)–7(f) and in Figs. 8(a) and 8(b) that, irrespectively on the thickness of LFO, J_{SC} and V_{OC} preserve their sign ($J_{SC} > 0$, $V_{OC} < 0$) for both electrodes, and the V_{OC} is definitely larger for BLSO than Pt. These observations are fully consistent with the VBOs derived from

XPS data [Figs. 4(c) and 4(d)]. That is, the positive $V_{BI,XPS}$ values in both LSMO/LFO/Pt and LSMO/LFO/BLSO means a built-in field pointing downwards from top electrode to bottom electrode, thus the photocurrent should flow downwards and be measured as positive value. On the other hand, V_{OC} is essentially, the voltage required to cancel the net current flowing in the circuit (open circuit voltage) and therefore it should have a sign opposite to V_{BI}. Therefore, as we determine $V_{BI} > 0$ for both devices, V_{OC} should also be negative, which is in agreement with experimental data (Fig. 7) as observed.

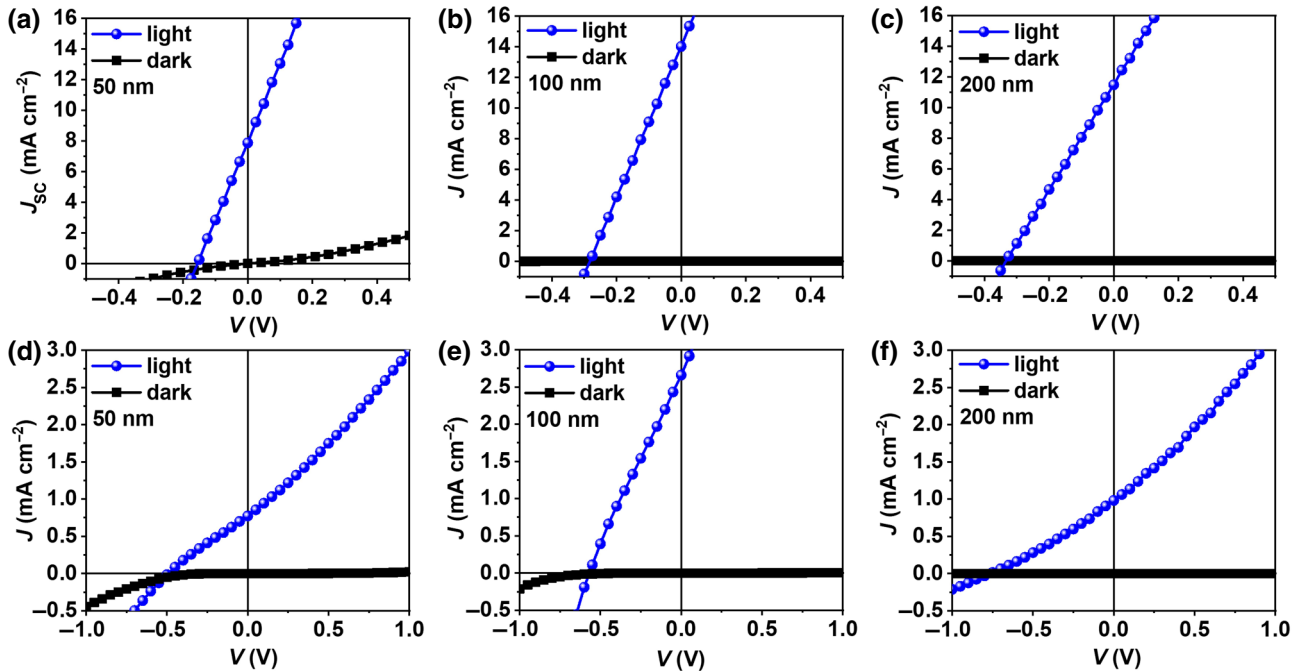From Figs. 5(c) and 5(d) it should be expected that V_{OC} values are roughly given by [52]

FIG. 7. J-V characteristics recorded in dark and under illumination on (a)–(c) LSMO/LFO/Pt and (d)–(f) LSMO/LFO/BLSMO where (a),(d) $t_{LFO} = 50$ nm, (b),(e) $t_{LFO} = 100$ nm, and (c),(f) $t_{LFO} = 200$ nm respectively.

$$V_{OC}(\text{LSMO/LFO/Pt}) \approx V_{BI}(\text{LSMO/LFO})$$
$$- V_{BI}(\text{LFO/Pt}), \qquad (4)$$

$$V_{OC}(\text{LSMO/LFO/BLSO})$$
$$\approx V_{BI}(\text{LSMO/LFO})$$
$$- [E_{VBM} - V_{BI}(\text{LFO/BLSO})], \qquad (5)$$

where E_{VBM} is the measured VBM energy of BLSO (approximately equal to -3.2 eV, Fig. S6.5 within the Supplemental Material [17]) referred to the Fermi level. Using the experimentally determined band-alignment values $V_{BI}(\text{LSMO/LFO}) \approx -0.75$ eV, $V_{BI}(\text{LFO/Pt}) \approx 0.86$ eV and $V_{BI}(\text{LFO/BLSO}) = -2.17$ eV, we deduce $V_{OC}(\text{LSMO/LFO/Pt}) = -0.11$ eV and $V_{OC}(\text{LSMO/LFO/BLSO}) = 0.28$ eV. The measured [Fig. 8(a)] and the predicted V_{OC} values (Eqs. (4) and (5)) [dashed lines in Fig. 8(a)] reveal some discrepancies, most noticeable for BLSO. They may have different sources. Most obvious is that V_{OC} is measured from photoresponse in LSMO/LFO/Pt and LSMO/LFO/BLSO devices where the active LFO layer and top electrodes have radically different thickness than those used for XPS, and therefore the determined VBO and E_{VBM} may not represent accurately enough the actual values in the devices. On the other hand, as mentioned, residual charging effects in LFO/BLSO band-alignment derivation (Table I) may still be present and lead to a spuriously large ΔE_{VBM} (approximately equal to -2.17 eV) that leads to an underestimation of the V_{OC} [Eq. (5)]. On the other hand, in the derivation of the band alignment from XPS data, we omit a possible role of a photovoltage induced by the x-ray beam, as documented in some metal-semiconductor heterostructures, which may contribute to the measured V_{BI} [40].

On the other hand, XPS band-alignment experiments have required the used of ultrathin LFO layers (1, 3, 5 nm). These ultrathin epitaxial films can be safely assumed to be homogeneous strained and thus any flexoelectric contribution to the internal field should be null and not contributing to the band alignment. In contrast, the photoresponse is measured in thicker LFO films (50, 100, 200 nm) where x-ray diffraction and STEM data confirm the presence of various possible sources of strain gradients of various gradient directions. The sign agreement between the relative VBO values derived from XPS and V_{OC} obtained from J-V indicates that band alignment in LSMO/LFO/Pt and LSMO/LFO/BLSO is dictated by intrinsic electronic effects rather by flexoelectric fields.

Data in Fig. 8(b) indicates that irrespectively on the top electrode, initially J_{SC} increases with t_{LFO} until reaching maxima at $t_{LFO} \approx 100$ nm: $J_{SC}(\text{Pt}) \approx 14$ mA cm^{-2} and $J_{SC}(\text{BLSO}) \approx 2.6$ mA cm^{-2}. From Fig. 6(b), the absorption coefficient at the 405-nm laser is $\alpha \approx 16$ µm^{-1} thus the light attenuates to approximately equal to 20% in the 100-nm light path. Accordingly, this initial increase of J_{SC} with t_{LFO} is attributed to the photoabsorption in LFO that itself increases with t_{LFO} until saturation. A further increase of t_{LFO} leads to a decrease to J_{SC} due to charge recombination within LFO, as observed. Data also indicates that J_{SC} is definitely larger when using Pt electrodes than when using BSLO. This difference, which cannot be accounted for by the different optical transparency of the electrodes (Pt is semitransparent but BLSO is virtually transparent at visible light), suggest that electron-hole recombination at LFO/BLSO interface is larger than at the LFO/Pt interface, precluding efficient charge extraction in the former. The high temperature growth of BLSO on top LFO compared to the room-temperature growth of Pt, can easily explain this difference.

Finally, it is observed in Fig. 8(a) that V_{OC} systematically increases with t_{LFO}. While some increase of V_{OC} with t_{LFO} is expected as in diodelike solar cells by $V_{OC} \approx \ln(J_{SC})$ [53], the absence of saturation in $V_{OC}(t_{LFO})$ suggests other contributions to V_{OC} that we comment in the following.
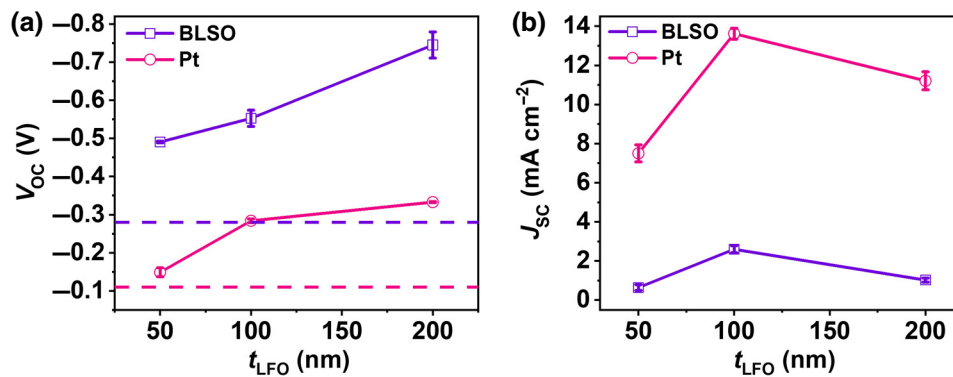

FIG. 8. Dependence of the (a) V_{OC} and (b) J_{SC} in LSMO/LFO/Pt (red circles) and LSMO/LFO/BLSO (purple squares), as a function of the thickness of LFO (t_{LFO}). The red (LSMO/LFO/Pt) and purple (LSMO/LFO/BLSO) dashed lines in (a) indicate the predicted V_{OC} as estimate from built-in voltages deduced from XPS data.

IV. DISCUSSION AND CONCLUSION

It is shown here that the photovoltaic response of LFO films of different thicknesses (50, 100, and 200 nm) grown on well-matched substrates (LSAT) and bottom electrodes (LSMO), largely differs depending on the top electrode used (here, Pt and BLSO). Band-alignment measurements strongly indicate that the V_{OC} is directly related to the built-in voltage at the top LFO/Pt and LFO/BLSO interfaces, which already manifests in the measured J-V curves in dark. BLSO electrodes establish a larger built-in potential than Pt. In contrast, they lead to a relatively smaller J_{SC} that we plausibly attribute to unavoidable chemical interdiffusion at the LFO/BLSO interface occurring during the high temperature growth, which is absent in the room-temperature grown LFO/Pt interface. On the other hand, the growth of $LaFeO_3$ (orthorhombic in bulk) thin films on cubic substrates leads to a complex microstructure where crystallites of different texture and strain state coexist and which relative abundance depends on thickness. Despite the minor epitaxial mismatch of LFO films grown on LSAT substrates ($<0.2\%$) epitaxial strain and strain relaxation is observed.

However, available data does not suggest any relevant impact of epitaxial strain gradients on the relative values of J_{SC}(LFO/Pt) and J_{SC}(LFO/BLSO) nor on the relative values of V_{OC}(LFO/Pt) and V_{OC}(LFO/BLSO) as microstructure of the underlying LFO is virtually identical. However, strain gradients may affect the absolute measured values V_{BI}(LFO/Pt) and V_{BI}(LFO/BLSO), as these data are collected using ultrathin LFO films whereas photoresponse is determined using thicker films where the presence of flexoelectric voltages cannot be excluded. In any event, it is remarkable that the measured J_{SC} value for the LSMO/LFO(100)/Pt device [J_{SC}(Pt)≈ 14 mA cm^{-2}] corresponds to a responsivity R ($=J_{SC}/I_0$) of 2.6×10^{-4} A W^{-1}. This responsivity value is larger than reported for thinner LFO films on $LaAlO_3$ substrates, where epitaxial strain and inhomogeneous strain relaxation are claimed to assist band-bending and charge extraction via flexoelectric fields [12]. The excellent room-temperature responsivity of LSMO/LFO/Pt heterostructures reported here, even larger than in the celebrated $BiFeO_3$ ($R = 1.5 \times 10^{-4}$ A W^{-1} [54]) and comparable to the responsivity of $BiFeO_3$ recorded at high temperature (66.1 °C) [55], suggesting that there is room for improvement and potential in application. Interestingly, the coexistence of differently textured crystallites in the LFO thin film does not appear to be detrimental but in contrast, they may be able to boost responsivity. Although at first sight counterintuitive, similar behavior has been documented in CdTe solar cells and other materials [56, 57]. In this scenario, even higher responsivity could be obtained if film microstructure and strain gradients can be engineered and combined with appropriate electrode selection.

ACKNOWLEDGMENTS

AUTHOR CONTRIBUTIONS

Y. Sheng and M. Mirjolet contributed equally to this work. J. Fontcuberta conceptualized and supervised the work. Y. Sheng and M. Mirjolet conducted the formal analysis and investigation. Y. Sheng, M. Mirjolet, M. Villa, J. Gàzquez, J. Santiso, and J. Fraxedas conducted the experiments and data curation. A. Klein conceptualized the band alignments.

[1] W. Lin, J. He, B. Ma, M. Matzelle, J. Xu, J. Freeland, Y. Choi, D. Haskel, B. Barbiellini, A. Bansil, *et al.*, Evidence for spin swapping in an antiferromagnet, Nat. Phys. **18,** 800 (2022).

[2] M. Nakamura, F. Kagawa, T. Tanigaki, H. S. Park, T. Matsuda, D. Shindo, Y. Tokura, and M. Kawasaki, Spontaneous Polarization and Bulk Photovoltaic Effect Driven by Polar Discontinuity in $LaFeO_3$/$SrTiO_3$ Heterojunctions, Phys. Rev. Lett. **116,** 156801 (2016).

[3] K. Nakamura, H. Mashiko, K. Yoshimatsu, and A. Ohtomo, Impact of built-in potential across $LaFeO_3$/$SrTiO_3$ heterojunctions on photocatalytic activity, Appl. Phys. Lett. **108,** 211605 (2016).

[4] R. Comes and S. Chambers, Interface Structure, Band Alignment, and Built-In Potentials at $LaFeO_3$/n−$SrTiO_3$ Heterojunctions, Phys. Rev. Lett. **117,** 226802 (2016).

[5] S. R. Spurgeon, P. V. Sushko, S. A. Chambers, and R. B. Comes, Dynamic interface rearrangement in $LaFeO_3$/n−$SrTiO_3$ heterojunctions, Phys. Rev. Mater. **1,** 063401 (2017).

[6] P. Zubko, G. Catalan, and A. K. Tagantsev, Flexoelectric effect in solids, Annu. Rev. Mater. Res. **43**, 387 (2013).

[7] D. Lee, A. Yoon, S. Y. Jang, J.-G. Yoon, J.-S. Chung, M. Kim, J. F. Scott, and T. W. Noh, Giant Flexoelectric Effect in Ferroelectric Epitaxial Thin Films, Phys. Rev. Lett. **107,** 057602 (2011).

[8] D. Lee, S. M. Yang, J. Yoon, and T. W. Noh, Flexoelectric rectification of charge transport in strain-graded dielectrics, Nano Lett. **12**, 6436 (2012).

[9] K. Chu, B.-K. Jang, J. H. Sung, Y. A. Shin, E.-S. Lee, K. Song, J. H. Lee, C.-S. Woo, S. J. Kim, S.-Y. Choi, *et al.*, Enhancement of the anisotropic photocurrent in ferroelectric oxides by strain gradients, Nat. Nanotechnol. **10**, 972 (2015).

[10] S. Das, B. Wang, T. R. Paudel, S. M. Park, E. Y. Tsymbal, L.-Q. Chen, D. Lee, and T. W. Noh, Enhanced flexoelectricity at reduced dimensions revealed by mechanically tunable quantum tunnelling, Nat. Commun. **10**, 537 (2019).

[11] M. Yang, D. J. Kim, and M. Alexe, Flexo-photovoltaic effect, Science **360**, 904 (2018).

[12] M. Wu, Z. Jiang, X. Lou, F. Zhang, D. Song, S. Ning, M. Guo, S. J. Pennycook, J. Dai, and Z. Wen, Flexoelectric thin-film photodetectors, Nano Lett. **21**, 2946 (2021).

[13] Z. Jiang, Z. Xu, Z. Xi, Y. Yang, M. Wu, Y. Li, X. Li, Q. Wang, C. Li, D. Wu, and Z. Wen, Flexoelectric-induced photovoltaic effects and tunable photocurrents in flexible LaFeO$_3$ epitaxial heterostructures, J. Mater. **8**, 281 (2022).

[14] S. M. Park, B. Wang, T. Paudel, S. Y. Park, S. Das, J. R. Kim, E. K. Ko, H. G. Lee, N. Park, L. Tao, *et al.*, Colossal flexoresistance in dielectrics, Nat. Commun. **11**, 2586 (2020).

[15] E. A. Kraut, R. W. Grant, J. R. Waldrop, and S. P. Kowalczyk, Precise Determination of the Valence-Band Edge in X-Ray Photoemission Spectra: Application to Measurement of Semiconductor Interface Potentials, Phys. Rev. Lett. **44**, 1620 (1980).

[16] E. A. Kraut, R. W. Grant, J. R. Waldrop, and S. P. Kowalczyk, Semiconductor core-level to valence-band maximum binding-energy differences: Precise determination by x-ray photoelectron spectroscopy, Phys. Rev. B **28**, 1965 (1983).

[17] See Supplemental Material at http://link.aps.org/supplemental/10.1103/PhysRevApplied.19.024001 for details of methods, structural data, transport model simulation, optical properties, valence-band offset determination, and the growth of LaFeO$_3$ single layers, which includes Refs. [58–71].

[18] S. M. Selbach, J. R. Tolchard, A. Fossdal, and T. Grande, Non-linear thermal evolution of the crystal structure and phase transitions of LaFeO$_3$ investigated by high temperature x-ray diffraction, J. Solid State Chem. **196**, 249 (2012).

[19] Z. Yu, D. A. Muller, and J. Silcox, Study of strain fields at A-Si/c-Si interface, J. Appl. Phys. **95**, 3362 (2004).

[20] P. J. Phillips, M. De Graef, L. Kovarik, A. Agrawal, W. Windl, and M. J. Mills, Atomic-resolution defect contrast in low angle annular dark-field STEM, Ultramicroscopy **116**, 47 (2012).

[21] A. J. Chiquito, C. A. Amorim, O. M. Berengue, L. S. Araujo, E. P. Bernardo, and E. R. Leite, Back-to-back Schottky diodes: The generalization of the diode theory in analysis and extraction of electrical parameters of nanodevices, J. Phys. Condens. Matter **24**, 225303 (2012).

[22] Z. Zhang, K. Yao, Y. Liu, C. Jin, X. Liang, Q. Chen, and L.-M. Peng, Quantitative analysis of current-voltage characteristics of semiconducting nanowires: Decoupling of contact effects, Adv. Funct. Mater. **17**, 2478 (2007).

[23] Z. Zhong and P. Hansmann, Band Alignment and Charge Transfer in Complex Oxide Interfaces, Phys. Rev. X **7**, 011023 (2017).

[24] A. Klein, Energy band alignment at interfaces of semiconducting oxides: A review of experimental determination using photoelectron spectroscopy and comparison with theoretical predictions by the electron affinity rule, charge neutrality levels, and the common anion, Thin Solid Films **520**, 3721 (2012).

[25] P. Lopez-Varo, L. Bertoluzzi, J. Bisquert, M. Alexe, M. Coll, J. Huang, J. A. Jimenez-Tejada, T. Kirchartz, R. Nechache, F. Rosei, and Y. Yuan, Physical aspects of ferroelectric semiconductors for photovoltaic solar energy conversion, Phys. Rep. **653**, 1 (2016).

[26] M. Minohara, I. Ohkubo, H. Kumigashira, and M. Oshima, Band diagrams of spin tunneling junctions La$_{0.6}$Sr$_{0.4}$MnO$_3$/Nb : SrTiO$_3$ and SrRuO$_3$/Nb : SrTiO$_3$ determined by in situ photoemission spectroscopy, Appl. Phys. Lett. **90**, 132123 (2007).

[27] M. Minohara, R. Yasuhara, H. Kumigashira, and M. Oshima, Termination layer dependence of Schottky barrier height for La$_{0.6}$Sr$_{0.4}$MnO$_3$/Nb : SrTiO$_3$ heterojunctions, Phys. Rev. B **81**, 235322 (2010).

[28] H.-S. Lee and H.-H. Park, Band structure analysis of La$_{0.7}$Sr$_{0.3}$MnO$_3$ perovskite manganite using a synchrotron, Adv. Condens. Matter Phys. **2015**, 1 (2015).

[29] G. N. Derry, M. E. Kern, and E. H. Worth, Recommended values of clean metal surface work Functions, J. Vac. Sci. Technol., A **33**, 060801 (2015).

[30] R. Schlaf, C. D. Merritt, L. A. Crisafulli, and Z. H. Kafafi, Organic semiconductor interfaces: discrimination between charging and band bending related shifts in frontier orbital line-up measurements with photoemission spectroscopy, J. Appl. Phys. **86**, 5678 (1999).

[31] B. E. Nieuwenhuys, O. G. Van Aardenne, and W. M. H. Sachtler, adsorption of xenon on group VIII and Ib metals studied by photoelectric work function measurements, Chem. Phys. **5**, 418 (1974).

[32] A. Klein, Interface properties of dielectric oxides, J. Am. Ceram. Soc. **99**, 369 (2016).

[33] A. Ohta, H. Murakami, S. Higashi, and S. Miyazaki, Determination of energy band alignment in ultrathin Hf-based oxide/Pt system, J. Phys. Conf. Ser. **417**, 012012 (2013).

[34] D. R. Lide, *Handbook of Chemistry and Physics*, 84th ed. (CRC Press LLC, Boca Raton, 2003).

[35] E. Y. Tsymbal and I. Žutić, *Spintronics Handbook: Spin Transport and Magnetism*, 2nd ed. (CRC Press, Taylor & Francis, Boca Raton, 2019).

[36] K. Krishnaswamy, L. Bjaalie, B. Himmetoglu, A. Janotti, L. Gordon, and C. G. Van de Walle, BaSnO$_3$ as a channel material in perovskite oxide heterostructures, Appl. Phys. Lett. **108**, 083501 (2016).

[37] J. D. Baniecki, T. Yamazaki, D. Ricinschi, Q. Van Overmeere, H. Aso, Y. Miyata, H. Yamada, N. Fujimura, R.

Maran, T. Anazawa, *et al.*, Strain dependent electronic structure and band offset tuning at heterointerfaces of $ASnO_3$ (A = Ca, Sr, and Ba) and $SrTiO_3$, Sci. Rep. **7,** 41725 (2017).

[38] S. A. Chambers, T. C. Kaspar, A. Prakash, G. Haugstad, and B. Jalan, Band alignment at epitaxial $BaSnO_3/SrTiO_3(001)$ and $BaSnO_3/LaAlO_3(001)$ heterojunctions, Appl. Phys. Lett. **108,** 152104 (2016).

[39] S. Lee, H. Wang, P. Gopal, J. Shin, H. M. I. Jaim, X. Zhang, S.-Y. Jeong, D. Usanmaz, S. Curtarolo, M. Fornari, *et al.*, Systematic band gap tuning of $BaSnO_3$ via chemical substitutions: The role of clustering in mixed-valence perovskites, Chem. Mater. **29,** 9378 (2017).

[40] R. Schafranek, S. Payan, M. Maglione, and A. Klein, Barrier height at $(Ba, Sr)TiO_3/Pt$ interfaces studied by photoemission, Phys. Rev. B **77,** 195310 (2008).

[41] J. R. Waldrop, R. W. Grant, S. P. Kowalczyk, and E. A. Kraut, Measurement of semiconductor heterojunction band discontinuities by x-ray photoemission spectroscopy, J. Vac. Sci. Technol., A **3,** 835 (1985).

[42] S. A. Chambers, M. H. Engelhard, V. Shutthanandan, Z. Zhu, T. C. Droubay, L. Qiao, P. V. Sushko, T. Feng, H. D. Lee, T. Gustafsson, *et al.*, Instability, intermixing and electronic structure at the epitaxial $LaAlO_3/SrTiO_3(001)$ heterojunction, Surf. Sci. Rep. **65,** 317 (2010).

[43] S. A. Chambers, L. Qiao, T. C. Droubay, T. C. Kaspar, B. W. Arey, and P. V. Sushko, Band Alignment, Built-In Potential, and the Absence of Conductivity at the $LaCrO_3/SrTiO_3(001)$ Heterojunction, Phys. Rev. Lett. **107,** 206802 (2011).

[44] R. Schafranek, S. Li, F. Chen, W. Wu, and A. Klein, $PbTiO_3/SrTiO_3$ Interface: Energy band alignment and its relation, Phys. Rev. B **84,** 045317 (2011).

[45] K. J. May, D. P. Fenning, T. Ming, W. T. Hong, D. Lee, K. A. Stoerzinger, M. D. Biegalski, A. M. Kolpak, and Y. Shao-Horn, Thickness-dependent photoelectrochemical water splitting on ultrathin $LaFeO_3$ films grown on Nb : $SrTiO_3$, J. Phys. Chem. Lett. **6,** 977 (2015).

[46] F. Chen, R. Schafranek, S. Li, W. B. Wu, and A. Klein, Energy band alignment between $Pb(Zr, Ti)O_3$ and high and low work function conducting oxides-from hole to electron injection, J. Phys. D: Appl. Phys. **43,** 295301 (2010).

[47] S. Li, C. Ghinea, T. J. M. Bayer, M. Motzko, R. Schafranek, and A. Klein, Electrical properties of $(Ba, Sr)TiO_3$ thin films with Pt and ITO electrodes: Dielectric and rectifying behaviour, J. Phys. Condens. Matter **23,** 334202 (2011).

[48] F. Chen, R. Schafranek, W. Wu, and A. Klein, Reduction-induced Fermi level pinning at the interfaces between $Pb(Zr, Ti)O_3$ and Pt, Cu and Ag metal electrodes, J. Phys. D: Appl. Phys. **44,** 255301 (2011).

[49] S. Y. Smolin, A. K. Choquette, R. G. Wilks, N. Gauquelin, R. Félix, D. Gerlach, S. Ueda, A. L. Krick, J. Verbeeck, M. Bär, *et al.*, Energy level alignment and cation charge states at the $LaFeO_3/LaMnO_3(001)$ heterointerface, Adv. Mater. Interfaces **4,** 1700183 (2017).

[50] A. P. N. Tchiomo, E. Carleschi, A. R. E. Prinsloo, W. Sigle, P. A. van Aken, J. Mannhart, P. Ngabonziza, and B. P. Doyle, Combined spectroscopy and electrical characterization of La : $BaSnO_3$ thin films and heterostructures, AIP Adv. **12,** 105019 (2022).

[51] Z. Lebens-Higgins, D. O. Scanlon, H. Paik, S. Sallis, Y. Nie, M. Uchida, N. F. Quackenbush, M. J. Wahila, G. E. Sterbinsky, D. A. Arena, *et al.*, Direct Observation of Electrostatically Driven Band Gap Renormalization in a Degenerate Perovskite Transparent Conducting Oxide, Phys. Rev. Lett. **116,** 027602 (2016).

[52] V. D. Mihailetchi, P. W. M. Blom, J. C. Hummelen, and M. T. Rispens, Cathode dependence of the open-circuit voltage of polymer:fullerene bulk heterojunction solar cells, J. Appl. Phys. **94,** 6849 (2003).

[53] W. Peter and W. Uni, Physics of solar cells: From principles to new concepts (2016).

[54] J. Xing, E.-J. Guo, J. Dong, H. Hao, Z. Zheng, and C. Zhao, High-sensitive switchable photodetector based on $BiFeO_3$ film with in-plane polarization, Appl. Phys. Lett. **106,** 033504 (2015).

[55] R. Zhao, N. Ma, K. Song, and Y. Yang, Boosting photocurrent via heating $BiFeO_3$ materials for enhanced self-powered UV photodetectors, Adv. Funct. Mater. **30,** 1906232 (2020).

[56] J. Chakrabartty, C. Harnagea, M. Celikin, F. Rosei, and R. Nechache, Improved photovoltaic performance from inorganic perovskite oxide thin films with mixed crystal phases, Nat. Photonics **12,** 271 (2018).

[57] I. Visoly-Fisher, S. R. Cohen, A. Ruzin, and D. Cahen, How polycrystalline devices can outperform single-crystal ones: Thin film CdTe/CdS solar cells, Adv. Mater. **16,** 879 (2004).

[58] D. Pesquera, *Strain and Interface-Induced Charge, Orbital and Spin Orderings in Transition-Metal Oxide Perovskites* (Universitat Autònoma de Barcelona, Bellaterra, 2014), http://hdl.handle.net/10803/283932.

[59] J. Walton, P. Wincott, N. Fairley, and A. Carrick, *Peak Fitting with CasaXPS: A Casa Pocket Book* (Accolyte Science, Knutsford, Cheshire, 2010).

[60] A. Grillo and A. Di Bartolomeo, A current–voltage model for double Schottky barrier devices, Adv. Electron. Mater. **7,** 2000979 (2021).

[61] F.-C. Chiu, A review on conduction mechanisms in dielectric films, Adv. Mater. Sci. Eng. **2014,** 1 (2014).

[62] C.-P. Kwan, M. Street, A. Mahmood, W. Echtenkamp, M. Randle, K. He, J. Nathawat, N. Arabchigavkani, B. Barut, S. Yin, *et al.*, Space-charge limited conduction in epitaxial chromia films grown on elemental and oxide-based metallic substrates, AIP Adv. **9,** 055018 (2019).

[63] F.-C. Chiu, H.-W. Chou, and J. Y. Lee, Electrical conduction mechanisms of metal/La_2O_3/Si structure, J. Appl. Phys. **97,** 103503 (2005).

[64] A. Goldenblum, I. Pintilie, M. Buda, A. Popa, T. Botila, A. Dimoulas, and G. Vellianitis, Space-charge-limited current involving carrier injection into impurity bands of high-k insulators, Appl. Phys. Lett. **86,** 203506 (2005).

[65] M. D. Scafetta, Y. J. Xie, M. Torres, J. E. Spanier, and S. J. May, Optical absorption in epitaxial $La_{1-x}Sr_xFeO_3$ thin films, Appl. Phys. Lett. **102,** 081904 (2013).

[66] T. Arima, Y. Tokura, and J. B. Torrance, Variation of optical gaps in perovskite-type 3d transition-metal oxides, Phys. Rev. B **48,** 17006 (1993).

[67] T. Arima and Y. Tokura, Optical study of electronic structure in perovskite-type RMO_3 (R = La, Y; M =

Sc, Ti, V, Cr, Mn, Fe, Co, Ni, Cu), J. Phys. Soc. Jpn. **64**, 2488 (1995).

[68] P. Decorse, E. Quenneville, S. Poulin, M. Meunier, A. Yelon, and F. Morin, Chemical and structural characterization of $La_{0.5}Sr_{0.5}MnO_3$ thin films prepared by pulsed-laser deposition, J. Vac. Sci. Technol., A **19**, 910 (2001).

[69] M. Descostes, F. Mercier, N. Thromat, C. Beaucaire, and M. Gautier-Soyer, Use of XPS in the determination of chemical environment and oxidation state of iron and sulfur samples: constitution of a data basis in binding energies for Fe and S reference compounds and applications to the evidence of surface species of an oxidized Py, Appl. Surf. Sci. **165**, 288 (2000).

[70] M. F. Sunding, K. Hadidi, S. Diplas, O. M. Løvvik, T. E. Norby, and A. E. Gunnæs, XPS characterisation of in situ treated lanthanum oxide and hydroxide using tailored charge referencing and peak fitting procedures, J. Electron Spectrosc. Relat. Phenom. **184**, 399 (2011).

[71] M. Björck and G. Andersson, GenX: An extensible x-ray reflectivity refinement program utilizing differential evolution, J. Appl. Crystallogr. **40**, 1174 (2007).